Li-storage and cycling properties of spinel, CdFe$_2$O$_4$, as an anode for lithium ion batteries[†]

YOGESH SHARMA, N SHARMA, G V SUBBA RAO and B V R CHOWDARI*

Department of Physics, National University of Singapore, 117542 Singapore

Abstract.   Cadmium ferrite, CdFe$_2$O$_4$, is synthesized by urea combustion method followed by calcination at 900°C and characterized by X-ray diffraction (XRD), scanning electron microscopy (SEM), high-resolution transmission electron microscopy (HR–TEM) and selected area electron diffraction (SAED) techniques. The Li-storage and cycling behaviour are examined by galvanostatic cycling, cyclic voltammetry (CV) and impedance spectroscopy in the voltage range, 0·005–3·0 V vs Li at room temperature. CdFe$_2$O$_4$ shows a first cycle reversible capacity of 870 ($\pm$ 10) mAhg^{-1} at 0·07C-rate, but the capacity degrades at 4 mAhg^{-1} per cycle and retains only 680 ($\pm$ 10) mAhg^{-1} after 50 cycles. Heat-treated electrode of CdFe$_2$O$_4$ (300°C; 12 h, Ar) shows a significantly improved cycling performance under the above cycling conditions and a stable capacity of 810 ($\pm$ 10) mAhg^{-1} corresponding to 8·7 moles of Li per mole of CdFe$_2$O$_4$ (vs theoretical, 9·0 moles of Li) is maintained up to 60 cycles, with a coulombic efficiency, 96–98%. Rate capability of heat-treated CdFe$_2$O$_4$ is also good: reversible capacities of 650 ($\pm$ 10) and 450 ($\pm$ 10) mAhg^{-1} at 0·5 C and 1·4 C (1 C = 840 mAg^{-1}) are observed, respectively. The reasons for the improved cycling performance are discussed. From the CV data in 2–15 cycles, the average discharge potential is measured to be ~0·9 V, whereas the charge potential is ~2·1 V. Based on the galvanostatic and CV data, *ex situ*-XRD, -TEM and -SAED studies, a reaction mechanism is proposed. The impedance parameters as a function of voltage during the 1st cycle have been evaluated and interpreted.

Keywords.   Li-storage; cycling properties; CdFe$_2$O$_4$; lithium ion batteries.

1.   Introduction

These are exciting times for the science and technology of nano-materials. Nano-size materials, whether they are elements, simple or complex compounds exhibit some special physical/chemical properties, in comparison to the bulk micron-size, due to the effects of 'quantum confinement' and large surface area to volume ratio. Thus, blue shift of the UV-visible absorption spectra of quantum dot structures, and oxide and chalcogenide semiconductors, surface magnetism, peculiar mechanical, electrical and dielectric properties, and enhanced catalytic and photo-catalytic activity have been realized in nano-structured materials. Some of these properties have been exploited for applications in a variety of devices.

Prof. C N R Rao is one of the first few to realize the novelty, significance and importance of the nano-materials for practical applications, and has been actively contributing to this frontier area for the past two decades (Rao and Gopalakrishnan 1986; Rao *et al* 2003, 2004, 2007a, b, c, 2009; Rao 2005; Rao and Govindaraj 2005; Rao and Kalyanikutty 2008). It is increasingly clear that nano-size materials will find niche applications in several areas of present-day interest like energy production, storage and

transport, pollution mitigation, green chemistry and environmental clean-up through catalysis and photo-catalysis. Indeed, as will be shown below, recent studies have shown that nano-size oxides and composites have been proven to be high-performance battery materials, and will find a place in the future-generation rechargeable batteries.

Commercial lithium ion batteries (LIBs), originally developed by Sony Co., Japan in 1991, use lithium cobalt oxide as the cathode (positive electrode) and graphite as the anode (negative electrode) material, and a non-aqueous Li-ion conducting electrolyte. The operating principle involves intercalation–de-intercalation of Li-ions, into/from the electrodes, to store and deliver electrical energy during charge–discharge process. LIBs possess high energy density with an operating voltage of 3·6 V, and are extensively used as the d.c. power sources in the present-day portable electronic appliances like cell phones, notebook computers and video camcorders (Nazri and Pistoia 2003; Tirado 2003; Armand and Tarascon 2008; Cheng *et al* 2008; Shukla and Kumar 2008). In order that they can be used in power tools, back-up power supplies and electric/hybrid electric vehicles (EV/HEV), three important criteria need to be met, viz. cost-reduction, improvement in the energy density and safety-in-operation at high current charge/discharge rates. To satisfy the above criteria, researches are being carried out worldwide to find alternative electrode mate-

rials based on cheap and environmentally-friendly compounds, and which may work on principles different from the Li- intercalation–de-intercalation reactions (Nazri and Pistoia 2003; Tirado 2003; Armand and Tarascon 2008; Shukla and Kumar 2008). As a result, we now have three prospective second-generation 4 V-cathodes, viz. the Li-containing mixed oxides, $Li(Ni_{1/3}Co_{1/3}Mn_{1/3})O_2$ (Manthiram *et al* 2006; Reddy *et al* 2006), $LiFePO_4$ (Padhi *et al* 1997; Saravanan *et al* 2009) and $LiVPO_4F$ (Huang *et al* 2009; Reddy *et al* 2009).

Researches on anodes for LIBs are directed towards materials which can form alloys with Li-metal (strictly, intermetallic compounds), and those undergoing redox ('conversion') reactions with Li (e.g. nano-CoO + Li ↔ nano-Co + Li_2O) (Nazri and Pistoia 2003; Tirado 2003; Armand and Tarascon 2008; Cheng *et al* 2008; Shukla and Kumar 2008). Metals like Sn, Zn and Cd form alloys with Li metal, and have been studied extensively as prospective anodes to replace the graphite in LIBs. The Li alloying–de-alloying reactions, which usually occur at low potentials ($\leq 1\cdot 0$ V vs Li) contribute to the reversible capacity during Li-cycling (e.g. $Sn + 4\cdot 4Li \leftrightarrow Li_{4\cdot 4}Sn$). Since metal oxides are easier to handle and process in comparison to the metals, they have also been explored in recent years, in the form of simple and complex oxides. In these cases, the oxides are first reduced to the respective metals by Li-metal under electrochemical conditions, followed by the Li-alloy formation.

Detailed studies have shown that the Li alloying–de-alloying reactions of Sn, Sb etc involve large changes in the unit cell volume, as high as 300% in some cases, and this is detrimental to the long-term Li-cyclability since it will give rise to 'electrochemical pulverization' of the active material of the electrode resulting in loss of electrical contact between the particles and with the current-collector, leading to the electrode disintegration and capacity-fading. Three approaches have been explored in order to mitigate the above electrode disintegration: (i) use of nano-size particles of the metals or oxides which will enable to absorb the volume changes due to the smaller number of atoms in the nano-grains and large surface area. Also, an increased access of Li to the alloy-forming metal particles and short diffusion path length for Li-ions will enable better electrode kinetics and current-rate capability, (ii) incorporation of one or more matrix elements, which are electrochemically active or inactive towards Li, like, Ca or Co. These can help in absorbing some of the volume changes of the main alloy-forming metal, improve the electronic conductivity of the composite, and also may act as catalysts for better Li-cycling and (iii) choice of the proper voltage range for Li-cycling. Using these guidelines, Sony Co., developed and introduced the amorphous-composite (Sn–Co–C) as the second-generation anode for LIBs (Sony Press News 2005).

Recently, we have shown that employing oxides like $ZnCo_2O_4$ (Sharma *et al* 2007a), $ZnFe_2O_4$ (Sharma *et al* 2008a), and $VSbO_4$ (Reddy *et al* 2008) or mixed-carbonate $(Cd_{1/3}Co_{1/3}Zn_{1/3})CO_3$ (Sharma *et al* 2009a) containing metal ions which can undergo Li-cycling via both alloying–de-alloying and conversion reactions, is a novel strategy to obtain large and stable capacities, and metal ions like Co and V are good matrix ions. Nano-size $ZnCo_2O_4$ shows a capacity of 900 (± 10) mAhg^{-1} stable at least up to 50 cycles when cycled at $0\cdot 1$ C-rate in the voltage range, $0\cdot 005$–$3\cdot 0$ V vs Li. The mechanism was shown to involve alloying–de-alloying (Zn + Li ↔ LiZn) and conversion (MO + Li ↔ M + Li_2O, M = Zn and Co) reactions.

As part of a comprehensive program of work on the suitability of metal oxides with the spinel structure, $A[B_2]O_4$ (A and B are metals) as prospective anode materials for LIBs, we have investigated the compounds, ACo_2O_4, A = Cu (Sharma *et al* 2007b), Fe, Mg (Sharma *et al* 2008b), Zn (Sharma *et al* 2007a), and $ZnFe_2O_4$ (Sharma *et al* 2008a). Presently, we have studied the Li-storage and cyclability of cadmium ferrite, $Cd[Fe_2]O_4$. Since Cd can form the alloy, Li_3Cd (Wang *et al* 1986), and also participate in conversion reaction (M = Cd) (Li *et al* 2008a) along with Fe (Reddy *et al* 2007; Sharma *et al* 2008a; Li *et al* 2008b), we can expect a reversible capacity corresponding to $9\cdot 0$ moles of Li per formula unit. Results show that, indeed, $8\cdot 7$ moles of Li (capacity, 810 (± 10) mAhg^{-1}) are cyclable when cycled at $0\cdot 07$C in the range, $0\cdot 005$–$3\cdot 0$ V at ambient temperature and the capacity is stable in the range 10–60 cycles with a coulombic efficiency, 96–98%. Good C-rate capability is also exhibited by $CdFe_2O_4$ in the above mentioned voltage range.

2. Experimental

Urea combustion method (Sharma *et al* 2007a, b, 2008a; Patil *et al* 2008) is employed to prepare $CdFe_2O_4$ using the raw materials, cadmium chloride, $CdCl_2 \cdot H_2O$ ($0\cdot 02$ M; Merck; >99%), NaOH ($0\cdot 04$ M; Merck; >98%) and Fe-oxalate·$2H_2O$ (Aldrich; >98%). Firstly, $CdCl_2$ was converted to the hydroxide, $Cd(OH)_2$ by aqueous precipitation with NaOH. It was filtered, washed with de-ionized water and then dried at 80°C for 12 h. The freshly prepared $Cd(OH)_2$ ($0\cdot 022$ M) and iron oxalate ($0\cdot 044$ M) were dissolved separately in minimum amount of conc. HNO_3. These nitrate solutions were mixed and kept at 80°C for 1h with continuous stirring. Urea ($0\cdot 132$ M; Aldrich; >99%) was added to the solution and heated slowly at 80–90°C for 12 h to evaporate the water. The dried powder was ground thoroughly using a mechanical grinder and calcined in air first at 400°C for 6 h and then at 900°C for 6 h. After cooling to room temperature, the powder was recovered, ground and kept in a desiccator. Structural and morphological characterizations were carried out using X-ray diffractometer (Philips, Expert) equipped with CuK$_\alpha$-radiation, scanning electron microscope, SEM (JEOL JSM-6700F, Field Emission Electron

Microscope), transmission electron microscope, TEM (JEOL JEM 3010 operating at 300 kV) and selected area electron diffraction (SAED) techniques.

For the electrochemical studies, the composite electrode is fabricated onto a Cu-current collector with the composition: $CdFe_2O_4$: binder (Kynar 2801): Super P carbon in the weight ratio of 70 : 15 : 15. A thick slurry of the above mixture was prepared using 1-methyl 2-pyrrolidone (NMP) as the solvent and coated onto an etched copper foil (thickness ~ 10–15 μm) using the doctor blade technique and was dried at 80°C in an air oven for 12 h to evaporate the solvent. The dried thick film (20–30 μm) electrode was pressed between stainless steel twin rollers to ensure an intimate contact of the active material to the current collector, followed by cutting it into circular discs (16 mm diameter). After drying the discs in a vacuum oven at 70°C for 12 h, they were transferred to an Ar-filled glove box, which maintains <1 ppm of H_2O and O_2 (MBraun, Germany). Coin cells (size, 2016: 20 mm dia. and 1·6 mm thick) were fabricated in the glove box using Li metal (Kyokuto Metal Co., Japan) foil as the counter electrode, Celgard 2502 membrane or glass micro-fibre sheet (Whatman, UK) as the separator and 1M $LiPF_6$ dissolved in ethylene carbonate (EC) and diethyl carbonate (DEC) or di-methyl carbonate (DMC) (1 : 1 by volume, Merck Selectipur LP40) as the electrolyte. The active material content in the electrode was ~ 3–4 mg and the electrode area was ~2 cm². Galvanostatic charge–discharge cycling and cyclic voltammetry studies were performed on several assembled cells after aging them for 24 h at ambient temperature ($RT \sim 25$°C) by computer-controlled Bitrode multiple battery tester (model SCN, Bitrode, USA) and Macpile II (Biologic, France), respectively. Electrochemical impedance spectroscopy was carried out using the Solartron Impedance/Phase-Gain analyzer (SI 1260) coupled with a battery tester unit (1470). An a.c. signal of 5 mV and the frequency varying from 0·1 MHz to 5 Hz were used to measure the impedance data. Data acquisition and analysis were carried out using the electrochemical impedance software, *Z* plot and *Z* view (Version 2.2, Scribner Associates Inc., USA). For *ex situ* -XRD, -TEM and -SAED studies, the cells were charged or discharged to a specific voltage and relaxed for 2 h and then they were disassembled inside the glove box. The composite electrodes containing the active material was recovered and washed thoroughly with the solvent, DEC, to remove the electrolyte and processed as described in our earlier reports (Sharma *et al* 2007a, 2008a).

3. Results and discussion

3.1 *Structural and morphological characterization*

In the urea combustion method of synthesis, the nitrate ion acts as the oxidizer and urea as the fuel. The reaction products are the finely divided metal oxides and evolu-

tion of gases, CO_2, N_2 and H_2O. The excess urea also decomposes to ammonia and other gases, but in the process ensures that agglomeration of the fine particles does not occur, and thus, nano-size oxides are obtained (Patil *et al* 2008). In favourable cases, at the calcination temperature of 400°C, the metal oxides combine to give the ternary oxide like, nano-$ZnCo_2O_4$ (Sharma *et al* 2007a). In the present study, CdO and Fe_2O_3 were obtained after heating to 400°C, and the single-phase $CdFe_2O_4$ could be obtained only after subsequent heat treatment at 900°C.

Figure 1a shows the XRD pattern of the composite electrode of bare-$CdFe_2O_4$. All the characteristic peaks correspond to the cubic-spinel structure and reveal that the compound is formed in pure-phase form. The lattice parameter is obtained by fitting the XRD pattern using TOPAS software (version 2.1). The derived value, $a = 8\cdot68(2)$ Å compares well with $a = 8\cdot7089$ Å reported in the JCPDS card # 79-1155. The agglomeration of particles of submicron size is seen in the SEM photograph of $CdFe_2O_4$ (figure 2a). The TEM photograph shows that the particle size is in the range of 100–200 nm (figure 2b). The SAED pattern displays the concentric rings overlapped by some diffused spots, indicating the pure-phase formation and well-crystallinity of $CdFe_2O_4$ (figure 2c). The interplanar distances (*d*-values) corresponding to these spots/rings are derived by measuring the diameter of two symmetric spots/rings about the centre. They are 3·1 ($\pm 0\cdot03$) Å, 2·60 ($\pm 0\cdot03$) Å, 2·50 ($\pm 0\cdot03$) Å and 1·78 ($\pm 0\cdot03$) Å. The derived *d*-values are attributable to the (220), (311), (222) and (422) planes of cubic-$CdFe_2O_4$ (JCPDS card # 79-1155), respectively. Thus, the SAED data complement the XRD results (figure 1a).

3.2 *Galvanostatic cycling*

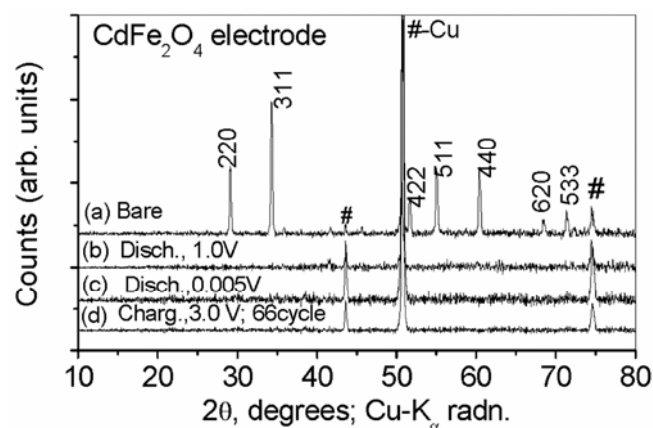Galvanostatic cycling in the range, 0·005–3·0 V vs Li at the constant current of 60 mAg^{-1} (0·07C) was carried out

Figure 1. XRD patterns of (**a**) bare electrodes of $CdFe_2O_4$, (**b**) discharged to 1·0 V, and (**c**) discharged to 0·005 V. (**d**) Heat-treated electrode charged to 3·0 V after 66 cycles. Lines due to $CdFe_2O_4$ along with Miller indices are shown. Lines due to Cu-substrate are shown.
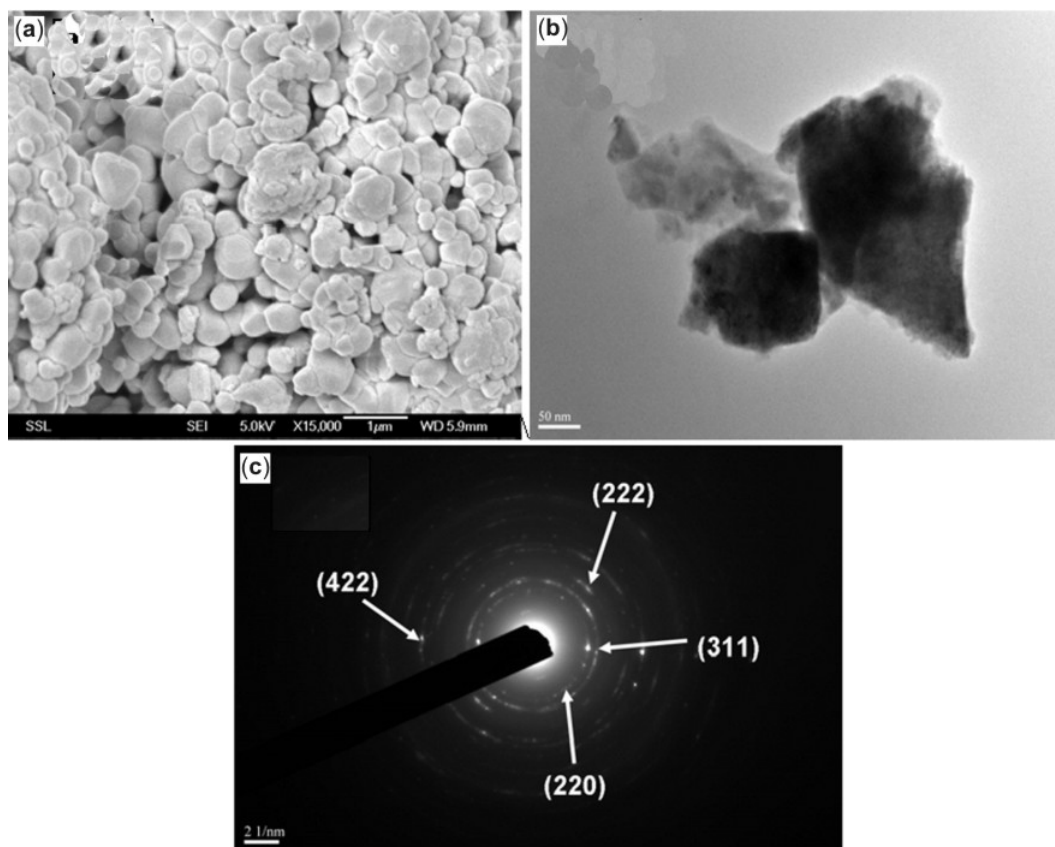
Figure 2. (**a**) SEM photograph of CdFe$_2$O$_4$. Agglomerates of sub-micron particles are clearly seen. Scale bar is 1 μm, (**b**) TEM image. Particles of size 100–200 nm are seen. Scale bar is 50 nm and (**c**) SAED pattern of bare-CdFe$_2$O$_4$. The assignment of the diffuse rings/spots to the different Miller indices of CdFe$_2$O$_4$ is shown. Scale bar is 2 nm^{-1}.
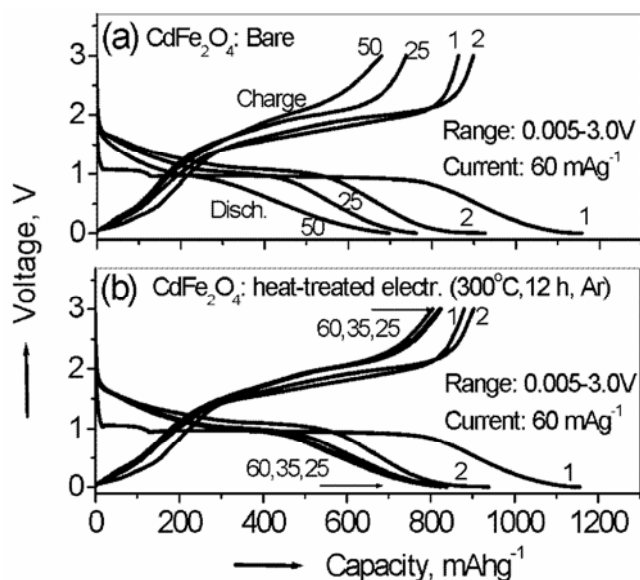

Figure 3. The voltage vs capacity profiles of CdFe$_2$O$_4$ in the voltage window, 0·005–3·0 V vs Li at the current rate of 60 mAg^{-1} (0·07C) at room temperature. (**a**) Bare (as prepared) electrode and (**b**) heat-treated (300°C for 12 h in Ar-atmosphere) electrode. Only selected cycles are shown for clarity. The numbers refer to the cycle number.

on the bare electrode of CdFe$_2$O$_4$ at *RT*. The voltage vs capacity profiles are shown in figure 3a. First discharge commences from the open circuit voltage (OCV ~ 2·8 V) and the cell voltage drops down quickly to ~ 1·1 V, followed by a large plateau region at ~ 1·0 V that extends to a capacity of 800 (± 10) mAhg^{-1}. This capacity corresponds to the consumption of ~ 8·6 moles of Li. After the voltage plateau region, the profile shows a gradual sloping region till the deep discharge voltage, 0·005 V. Thus, at the end of first discharge, a total capacity of 1180 (± 10) mAhg^{-1} is observed (consumption of 12·7 moles of Li per mole of CdFe$_2$O$_4$). The first charge (Li-extraction) profile from 0·005 to 3·0 V shows a small plateau at ~ 0·5 V followed by a continuous increase to 1·4 V. Beyond this, a broad plateau region occurs in the range, 1·5–2·0 V, and thereafter, a significant polarization of the electrode in the form of vertical profile is observed. The total first charge capacity, 870 (± 10) mAhg^{-1}, corresponds to the extraction of ~ 9·4 moles of Li per formula unit. The difference between discharge and charge capacities in the first cycle, viz. the irreversible capacity loss (ICL) is thus 26%.

The voltage–capacity profile of the 2nd discharge slightly differs from the first-discharge in that the voltage

decreases continuously from ~1·8 V and a smaller extent of voltage–plateau at ~1·0 V followed by the sloping region is seen (figure 3a). The total second-discharge capacity is 940 (± 10) mAhg⁻¹. The corresponding second-charge profile resembles qualitatively that of the first-charge except that the capacity value increases slightly to 900 (± 10) mAhg⁻¹. The voltage-capacity profiles are almost identical in the range, 2–50 discharge–charge cycles but show a continuous decrease in the capacity (figure 3a). To illustrate the Li-cyclability of $CdFe_2O_4$, the capacity vs cycle number plot is drawn from the galvanostatic cycling data and is shown in figure 4a. As can be seen, the reversible capacity decreases gradually till 15 cycles, and thereafter at a rate of ~3 mAhg⁻¹ per cycle till 50 cycles. At the 50th cycle, a reversible capacity of 680 (± 10) mAhg⁻¹ (7·3 moles of Li) is measured.

Recently, Dahn's group (Li *et al* 2008b) showed that a significant increase in the reversible capacity as well as cycling stability of the oxide, Fe_2O_3, can be achieved by heat treating the composite electrode, containing the active material, binder and conducting carbon, at 300°C for 12 h in argon, followed by cooling. Thus, while the bare electrode gave a reversible capacity of 400 mAhg⁻¹, the heat-treated electrode showed a capacity of ~800 mAhg⁻¹, stable up to at least 100 cycles, when cycled at 0·2C-rate in the voltage range, 0·005–3·0 V. This dramatic improvement in the electrode performance is ascribed to a better binder distribution, caused by the melting and spreading of the binder, followed by adhesion to the

active material particles and to the Cu-current collector. Presently, the composite electrode of $CdFe_2O_4$ is heat-treated under similar conditions and tested for Li-cyclability. The results are shown in the form of voltage vs capacity and capacity vs cycle number plots in figures 3b and 4a, respectively. As can be seen, the Li-cycling behaviour of heat-treated electrode is almost identical to that of bare electrode of $CdFe_2O_4$ (figures 3a, b and 4a) up to 10–15 cycles, displaying good reproducibility of Li-cycling response. However, in contrast to the bare-$CdFe_2O_4$ electrode which showed capacity-fading, the heat-treated electrode gives a stable capacity, 810 (±10) mAhg⁻¹ in the range of 10–60 cycles, which corresponds to 8·7 moles of cyclable Li. This shows that the heat-treatment of the composite electrode, indeed, has a beneficial effect on the cycling behaviour and corroborates the conclusions of Li *et al* (2008b). The SEM photographs of the bare and heat-treated composite electrode (figure not shown) indicate that the latter possesses smaller number of pores and un-coated portions, and denser packing of the active material and carbon particles, in comparison to the bare electrode.

Rate capability of heat-treated electrode of $CdFe_2O_4$ is also examined at various current rates in the range of 0·005–3·0 V vs Li. The capacity vs cycle number plot, shown in figure 4b, indicates that the capacity values are fairly stable at each C-rate from 0·12 C to 1·4 C, assuming 1 C = 840 mAg⁻¹. Capacities of 650 (± 10) mAhg⁻¹ at 0·5 C in the range 15–38 cycles, and 450 (± 10) mAhg⁻¹ at 1·4 C in the range, 56–75 cycles are observed. We note that these values are quite higher than the theoretical capacity of graphite (~372 mAhg⁻¹). When the C-rate is decreased, in steps from 1·4 C to 0·24 C, the reversible capacity values increased, as can be expected, but complete recovery is not seen (figure 4b).

3.3 *Ex situ XRD, TEM and SAED studies*

Ex situ-XRD, -TEM and -SAED studies were performed to investigate the nature of product formed upon Li-cycling. The XRD patterns of the bare electrodes of $CdFe_2O_4$, after discharge to 1·0 V and 0·005 V, and that of the heat-treated electrode after charging to 3·0 V after 66 cycles are shown in figures 1b–d. The characteristic peaks of cubic $CdFe_2O_4$, seen in the bare electrode, disappear at 1·0 V and only peaks due to substrate, Cu are seen. This indicates that the crystal structure destruction or amorphization of crystal lattice of $CdFe_2O_4$ occurs at ~1·0 V. The XRD patterns of the electrode which was discharged to 0·005 V and that of the charged electrode to 3·0 V after 66 cycles also are similar to the above which indicates that the product formed in the fully discharged (0·005 V) and charged (3·0 V) states are either amorphous in nature or nano-phase which have crystallite size smaller than the coherence length of X-rays.
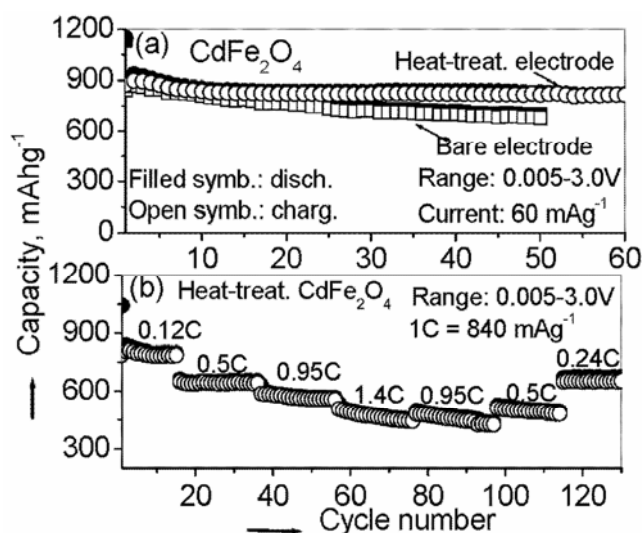

Figure 4. (**a**) The capacity vs cycle number plots in the voltage range, 0·005–3·0 V at the current of 60 mAg⁻¹ (0·07 C) (1C = 840 mAg⁻¹) for bare and heat-treated electrode of $CdFe_2O_4$. The filled and open symbols represent discharge and charge capacities, respectively and (**b**) capacity vs cycle number plot in the voltage range, 0·005–3·0 V at various current (*C*) rates of heat-treated electrode of $CdFe_2O_4$. For clarity, data for selected *C*-rates are shown. Filled and open symbols correspond to discharge- and charge-capacities, respectively.

To investigate further the products formed upon charging the bare electrode of $CdFe_2O_4$ to 3·0 V after 50 charge–discharge cycles, the HR–TEM and SAED studies were performed on the material recovered after disassembling the cell. Figure 5a shows the HR–TEM lattice image in which the dispersion of nano-crystalline regions (size, 5–10 nm) in the amorphous regions is seen. Some
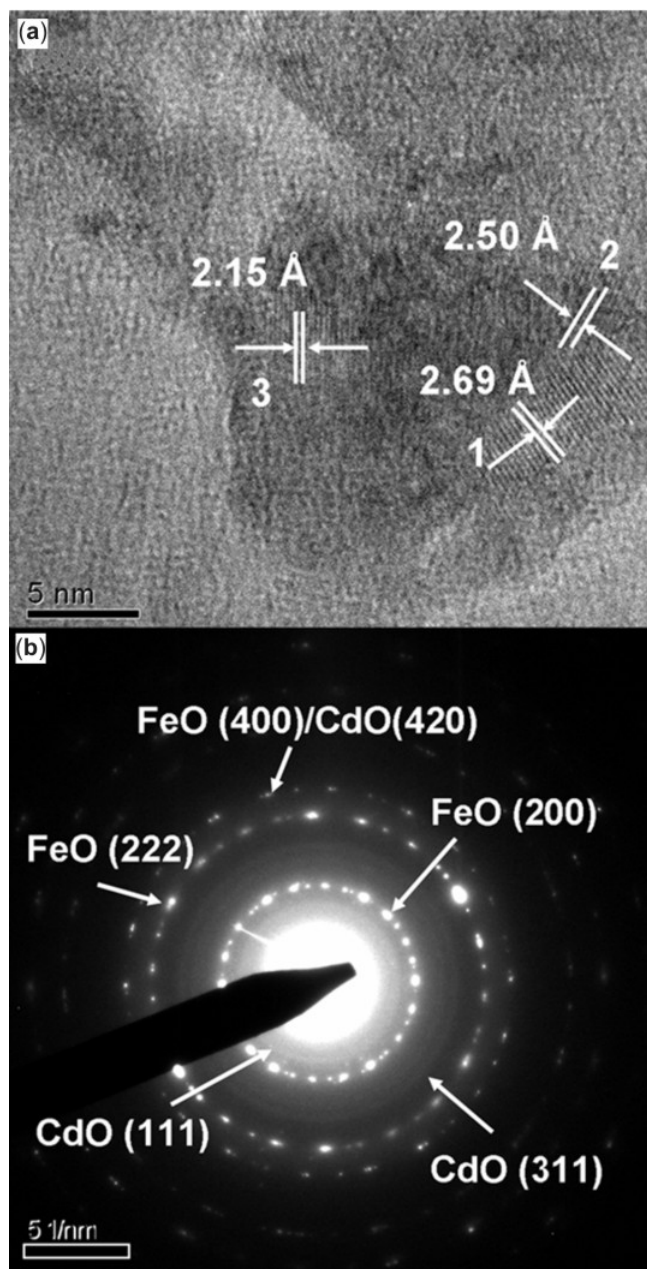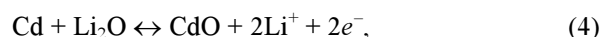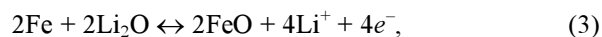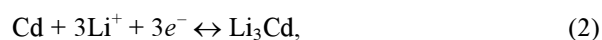

of these crystalline regions are marked as 1, 2 and 3. The interplanar distances (*d*-values) corresponding to these regions are: 2·69 (± 0.03) Å, 2·50 (± 0.03) Å and 2·15 (± 0.03) Å, respectively. The first value is attributed to the (111) plane of cubic-CdO ($a = 4.6953$ Å; JCPDS card # 05-0640), and the latter two can be assigned to the (111) and (200) planes of cubic-FeO ($a = 4.284$ Å; JCPDS card # 74-1881). In the SAED pattern (figure 5b), various diffuse spots superimposed on the concentric rings are seen that indicates the dispersion of nano-crystalline regions in the amorphous matrix and complements the lattice image data (figure 5a). The derived interplanar distances (± 0.03 Å) are: 2·70 Å, 2·49 Å, 2·13 Å, 1·23 Å and 1·09 Å. The first three values are almost same as found in the lattice image (figure 5a) and therefore, assigned accordingly to CdO and FeO. The last two values can be attributed to (222) and (400) planes of FeO, respectively. In addition, the *d*-values of 1·09 (± 0.03) Å can possibly be assigned also to the (420) plane of CdO. Thus, the products formed upon charging the bare electrode of $CdFe_2O_4$ to 3·0 V after 50 cycles are cubic-CdO and -FeO. From the *ex situ*-XRD, -TEM and -SAED data on the cycled electrodes, we conclude that the amorphous product consists of nano-size grains of mixture of CdO and FeO. There is no evidence for the re-formation of $CdFe_2O_4$ as is clear from the SAED patterns of figures 2c and 5b.

3.4 *Reaction mechanism*

On the basis of the observed reversible capacity values, *ex situ*-XRD, -TEM and -SAED studies, and similarity between the cycling behaviour of presently studied $CdFe_2O_4$ with the other reported Fe-based oxides like AFe_2O_4 (A = Zn, Co, Ni) (NuLi *et al* 2004; Lavela and Tirado 2007; Sharma *et al* 2008a) and Fe_2O_3 (Larcher *et al* 2003; Chen *et al* 2005; Morales *et al* 2005; Reddy *et al* 2007; Li *et al* 2008b), the following Li-storage and cycling mechanism can be proposed (1–4). The first-discharge reaction of $CdFe_2O_4$ with Li

$$CdFe_2O_4 + 8Li^+ + 8e^- \rightarrow Cd + 2Fe + 4Li_2O$$
$$(e = \text{electron}), \qquad (1)$$

$$Cd + 3Li^+ + 3e^- \leftrightarrow Li_3Cd, \qquad (2)$$

$$2Fe + 2Li_2O \leftrightarrow 2FeO + 4Li^+ + 4e^-, \qquad (3)$$

$$Cd + Li_2O \leftrightarrow CdO + 2Li^+ + 2e^-, \qquad (4)$$

involves the crystal structure destruction and amorphization of the lattice followed by the formation of nano-metal particles of Cd and Fe embedded in an amorphous-Li_2O matrix as per the forward reaction of (1) and thus, the consumption of 8·0 moles of Li per mole of $CdFe_2O_4$. This is depicted by a large voltage plateau seen in the
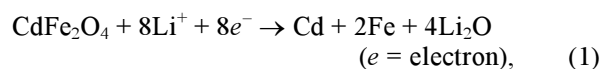
Figure 5. *Ex situ* TEM of bare electrode of $CdFe_2O_4$ charged to 3·0 V after 50 cycles. (**a**) High resolution lattice image showing the presence of nano-crystalline regions (5–10 nm) dispersed in amorphous region, marked as 1, 2 and 3. The derived interplanar spacings (± 0.03) Å are: 2·69 Å, 2·50 Å and 2·15 Å, respectively. Scale bar, 5 nm and (**b**) the corresponding SAED pattern. The diffuse spots/rings are assigned to the cubic CdO and FeO. Miller indices are shown. Scale bar, 5 nm^{-1}.

capacity–voltage profiles at ~1·0 V in figure 3a and supported by *ex situ* XRD data (figure 1), and indicates a two-phase reaction. The observed capacity of 800 (±10) mAhg⁻¹ (8·6 moles of Li) up to the end of plateau region agrees fairly well with the expected value. Below the voltage–plateau region, the freshly formed Cd metal reacts with Li to form the alloy, Li_3Cd as per the forward reaction of (2). The Li–Cd formation may occur in stages and therefore, no clear-cut voltage plateau, attributable to the alloying reaction is seen. This is in tune with the literature data where the completion of alloy formation to give Li_3Cd occurs in the voltage range, 0·6–0·2 V vs Li (Sharma *et al* 2009a, b). Thus, theoretically 11·0 moles of Li per mole of $CdFe_2O_4$ must be consumed during the first discharge process; however, the experimentally observed capacity corresponds to 12·7 moles of Li. This extra consumption of 1·7 moles of Li can be attributed partly to the solid electrolyte interphase (SEI) formation at the interface of electrode and electrolyte (Nazri and Pistoia 2003; Tirado 2003; NuLi *et al* 2004; Reddy *et al* 2007; Sharma *et al* 2007a, 2008a) and partly to the polymeric gel-type layer formed on the nano-particles of Fe-metal and the alloy during deep discharge to 0·005 V (Larcher *et al* 2003; Sharma *et al* 2008a).

The first-charge reaction involves the de-alloying reaction of Li_3Cd to give Cd metal as per the backward reaction of (2) and the corresponding voltage plateau is observed at ~0·3–0·5 V. In the case of pure CdO, results show that the de-alloying reaction of (2) occurs in two stages, at ~0·4 V and ~0·8 V vs Li (Sharma *et al* 2009b). The oxidation of Fe to FeO and Cd to CdO as per the forward reaction of (3) and (4), respectively occur in the voltage range, ~1·5–2·0 V according to the voltage plateaux (the first-charge profiles in figures 3a, b). The formation of nano-CdO and nano-FeO in the charged-state is confirmed on the basis of *ex situ*-TEM and -SAED studies, and also by the similarity between the voltage plateau regions of presently studied $CdFe_2O_4$ with those exhibited by other Fe-based oxides (NuLi *et al* 2004; Chen *et al* 2005; Sharma *et al* 2008a) and CdO (Li *et al* 2008a; Sharma *et al* 2009b). It may be mentioned that in some reports, the oxidation of iron, partly or fully to Fe^{3+} via FeO to give Fe_2O_3 in the final product upon completion of the charge reaction was also observed (NuLi *et al* 2004; Chen *et al* 2005; Morales *et al* 2005). However, Fe_2O_3 formation is not noticed in the present study from *ex situ*-TEM and -SAED studies. As per (2)–(4), 9·0 moles of Li are to be released during the first charge reaction to 3·0 V, which compares well with the experimentally observed 9·4 moles of Li. Slight excess of 0·4 mole of Li released may possibly be attributed to the contribution from the dissolution of polymeric layer (Grugeon *et al* 2003; Sharma *et al* 2008a). The observed stable cycling response of heat-treated electrode of $CdFe_2O_4$ with a capacity of 810 (±10) mAhg⁻¹ at 0·07 C can be ascribed to the nano-composite nature of the first discharge reaction

product and the role of (Li₃Cd–Cd–CdO) and (Fe–FeO) as mutually beneficial matrices in an amorphous matrix of Li_2O for the reversible reactions of (2)–(4). In addition, a more homogeneous distribution of active material in the conducting matrix of carbon facilitated by heat-treatment and thereby good buffering ability of volume variation involved in the electrochemical processes, ensured an improved Li-cycleability.

Under analogous cycling conditions of the voltage range, the Li-cycling performance of $CdFe_2O_4$ is superior to that of bulk and thin films of $ZnFe_2O_4$ (NuLi *et al* 2004; Sharma *et al* 2008a), sol–gel derived $NiFe_2O_4$ and $CoFe_2O_4$ (Lavela and Tirado 2007), and can be attributed to the participation of the alloy (Li_3Cd) in the reaction. We note that in the case of $ZnFe_2O_4$, the alloy (LiZn) only participates (Wang *et al* 1986; NuLi *et al* 2004; Sharma *et al* 2008a), whereas in other two cases, Ni and Co do not form alloys with Li.

3.5 *Cyclic voltammetry*

To discern the average discharge and charge potential during cycling, cyclic voltammetry studies were carried out on the heat-treated $CdFe_2O_4$ electrode in the potential range, 0·005–3·0 V at the slow scan rate, 58 µVs⁻¹. The Li metal was used as the reference and working electrode. The cyclic voltammograms (CVs) are shown in figure 6. The first discharge (cathodic) scan commences from the OCV (~2·7 V) to the deep discharge limit, 0·005 V and shows an intense peak at ~0·75 V with a small shoulder peak at 1·0 V which can be attributed to the two-phase reaction due to crystal structure destruction followed by the nano-metal particle formation embedded into the Li_2O matrix (1) (figure 6a). Since the alloy (Li_3Cd) formation occurs in stages, well-defined peaks attributable to the alloying reaction (forward reaction of (2)) are not seen. Nevertheless, a sloping tail in the CV up on deep discharge to 0·005 V is noticed that can be attributed to the completion of the Li_3Cd formation.

The anodic scan (Li-extraction) shows a small hump in the range 0·1–0·4 V that can be ascribed to the de-alloying reaction of (Li–Cd) that gives Cd metal in stages as per the backward reaction of (2). Further, a broad hump containing two discernible peaks at ~1·6 V and ~2·0 V is seen in the CV. These peaks can be attributed to the FeO and CdO formations and are in good agreement with the values reported in the literature for the Fe-based and Cd-based oxides (Sharma *et al* 2008a; Li *et al* 2008a; Sharma *et al* 2009b). The shape of the second cathodic CV is different from that of the first scan indicating a different reaction mechanism and shows a broad hump at ~1·4 V, and a well-defined peak centred at ~1·0 V. These can be ascribed to the reduction of newly formed CdO and FeO, respectively to the respective metals. The 2nd anodic CV is qualitatively similar to the first cycle CV except that

the broad peaks are shifted to ~1·7 V and ~2·1 V. The peak positions and intensities varied slightly during 2–5 cycles, and thereafter, almost overlapping of the CVs are seen that indicates good reversibility of Li–CdFe$_2$O$_4$ system as per the reversible reactions of (2)–(4) (figure 6a).

The CVs recorded after subjecting the CdFe$_2$O$_4$ electrode galvanostatically to 60 cycles, at 60 mAg^{-1} in the range 0·005–3·0 V, are shown in figure 6b. As can be seen, the 61–66 cycle CVs overlap well, indicating good reversibility of the discharge–charge reactions. The broad and well-spread humps displayed in both the cathodic and anodic scans indicate that the Li-cycling is occurring in the homogeneously-distributed nano-size particles. It is concluded that CV studies complement the galvanostatic cycling and proposed reaction mechanism, and from the CVs in the range 2–15 cycles, the average discharge and charge potentials are ~0·9 V and ~2·1 V, respectively in the CdFe$_2$O$_4$, and they pertain to (3) and (4).

3.6 *Electrochemical impedance spectroscopy (EIS)*

EIS studies have been carried out on the bare-CdFe$_2$O$_4$ electrode vs Li to obtain information on the electrode reaction kinetics. The cell was galvanostatically discharged or charged to a fixed voltage and relaxed at that voltage for 2 h, and the impedance data were collected during the 1st discharge–charge cycle. The results in the form of N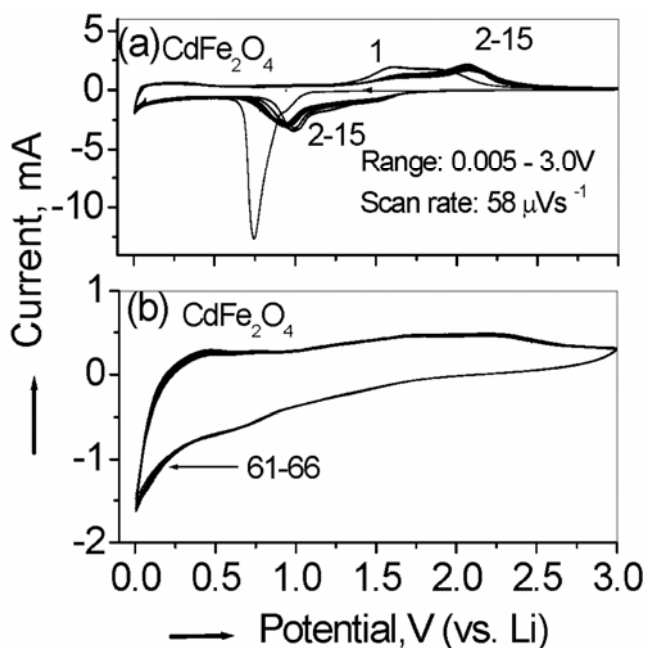yquist plots (Z' vs $-Z''$) are shown in figures 7a, b, where Z' and Z'' refer to the real and imaginary parts of cell impedance. The experimental data is fitted with an equivalent circuit shown in figure 7c which consists of a series and parallel combination of resistances, constant phase elements (CPEs) and Warburg impedance, W. The overall impedance is a summation of resistances offered by the electrolyte (e), surface film (sf), charge transfer (ct), bulk (b) and Warburg impedance. The corresponding constant phase elements are CPE$_{(sf)}$, CPE$_{(dl)}$ and CPE$_{(b)}$ where dl refers to double layer. The experimental data are shown as symbols whereas the fitting represents the continuous line in figures 7a, b. The CPEs are used instead of pure capacitor due to the depressed semicircle seen in the Nyquist plots that indicates the deviation from the ideal behaviour of a capacitor. The impedance of CPE can be derived from the equation, $Z_{CPE} = 1/[C_i(j\omega)^n]$, where $j = (-1)^{1/2}$, ω is the angular frequency, C_i the capacitance and n a constant which gives the extent of distortion. For a pure capacitor, $n = 1$ (Reddy *et al* 2007; Sharma *et al* 2008b).

The electrolyte resistance, R_e, was found to be 3·5 ($\pm$0·5) Ω irrespective of the state of charge and discharge of the cell. Under the OCV condition, the Nyquist plot shows a single semicircle in the range, 100 kHz–10 Hz followed by a sloping line (~45°) which turns to an almost vertical line from the *x*-axis. The semicircle is fitted by single R||CPE combination which can be attributed to

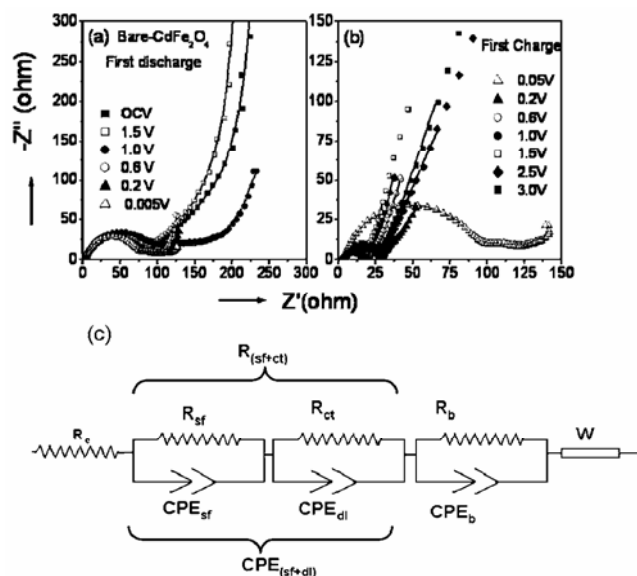**Figure 6.** (**a**) Cyclic voltammograms (CVs) of heat-treated CdFe$_2$O$_4$ in the potential window, 0·005–3·0 V vs Li at the slow scan rate of 58 μVs^{-1}. Li metal was the counter and reference electrode. The numbers indicate the cycle number and (**b**) the CVs during 61–66 cycles. The cell was first subjected to 60 cycles galvanostatically at 0·07 C-rate in the range, 0·005–3·0 V and the CVs were recorded.

Figure 7. Family of Nyquist plots (Z' vs $-Z''$) of the CdFe$_2$O$_4$–Li system at different voltages. (**a**) During the first-discharge reaction from open circuit voltage (OCV ~ 2·8 V), (**b**) during the first-charge reaction. The voltages at which the data were collected are shown. Symbols represent the experimental data and continuous lines indicate the fitting with the equivalent circuit of figure 7c. Geometric area of the electrode is ~2 cm^2 and the active mass in the electrode is ~ 3–4 mg and (**c**) equivalent circuit used for fitting the impedance spectra of figures 7a, b. Different resistances, R$_i$ and/or R$_i$||CPE$_i$ components and the Warburg element, W are shown.

surface film contribution. The derived values of R$_{sf}$ and CPE$_{sf}$ are 95($\pm$5) Ω and 24 ($\pm$2) μF, respectively. These values decrease slightly to 85 ($\pm$ 5) Ω and 22 ($\pm$ 2) μF, respectively at 1·5 V. The spectrum was fitted to a single semicircle but the charge transfer contribution has been taken into account for fitting, and thus the resistance and CPE are R$_{(sf + ct)}$ and CPE$_{(sf + dl)}$, respectively. At 1·0 V, the spectrum shows a significant change. The spread of the first semicircle slightly increases and an undeveloped semicircle (almost a straight line parallel to the *x*-axis) is seen, which is an indication of contribution from the bulk resistance to the overall impedance (figure 7a). Accordingly, the impedance data is fitted with two R∥CPE elements shown in figure 7c. The derived values of R$_{(sf + ct)}$ and R$_b$ are 84 ($\pm$ 5) and 102 ($\pm$ 5) Ω, respectively, and the corresponding CPE$_{(sf + dl)}$ = 15 ($\pm$ 3) μF and CPE$_b$ = 4 ($\pm$ 1) mF. As more and more Li reacts with CdFe$_2$O$_4$, the R$_{(sf + ct)}$ and CPE$_{(sf + dl)}$ values remain almost stable in the voltage range of 0·6 V to 0·005 V (R$_{(sf + ct)}$ = 64 ($\pm$ 4) Ω and CPE$_{(sf + ct)}$ = 14 μF) (figure 7a). The R$_b$ now decreases from 102 Ω at 1·0 V to 42 Ω at 0·6 V to 33 Ω at 0·2 V but increases to 49 Ω at 0·005 V. The corresponding values of CPE$_b$ remain almost constant at 6 ($\pm$ 1) mF. The values of *n* ($\pm$ 0·02) change gradually from 0·78 to 0·84 during the first-discharge process.

During the first charge, the Nyquist plot taken at 0·05 V is qualitatively the same as that obtained at 0·005 V during first discharge (figure 7b). The impedance parameters are: R$_{(sf + ct)}$ = 82 ($\pm$5) Ω, and corresponding CPE$_{(sf + dl)}$ = 16 ($\pm$ 3) μF, R$_b$ = 47 ($\pm$ 5) Ω, CPE$_b$ = 10 ($\pm$ 2) mF. However, at 0·2 V, the spectrum changes significantly in that the spread of the first-semicircle reduces considerably and the contribution from bulk impedance is also reduced significantly. Hence, the spectrum is fitted to a single semicircle. The R$_{(sf + ct)}$ is only 24 ($\pm$ 5) Ω with CPE$_{(sf + dl)}$ = 25 ($\pm$5) μF. The decreasing trend in the R$_{(sf + ct)}$ and increasing trend in the CPE$_{(sf + dl)}$ values continues up to 1·5 V during charge (figure 7b). Thus, in the range, 0·6–1·5 V, the R$_{(sf + ct)}$ = 16 ($\pm$ 1) Ω whereas the CPE$_{(sf + dl)}$ varies from 110 ($\pm$ 10) μF to 280 ($\pm$ 10) μF. Thereafter, the R$_{(sf + ct)}$ increases slowly to 28 ($\pm$ 1) Ω and CPE$_{(sf + dl)}$ = 290 ($\pm$ 10) μF at 2·5 V and 3·0 V. The contribution from R$_b$ is absent. The slight increase in R$_{(sf + ct)}$ values at V $\geq$ 2·5 V can be ascribed to the formation of metal oxides from the Fe- and Cd-metal nano-particles through the 'conversion' reactions (3 and 4). Also, for V > 2·0 V, the dissolution of polymeric layer takes place that causes the surface film impedance to decrease, but the charge transfer impedance increases. The *n* value decreases gradually from 0·81 at 0·05 V to 0·6 at 3·0 V during first charge process. To summarize, the R$_{(sf + ct)}$ varies from ~ 84 Ω to ~ 16 Ω during the first discharge–charge cycle. The contribution from R$_b$ to the overall impedance is seen only for V $\leq$ 1·0 V during the first-discharge and its value decreases from 102 Ω at 1·0 V to 49 Ω at 0·005 V. During the first-charge, R_b contribution is seen only at

V = 0·05 V, with a value of 47 Ω. These low values of R$_{(sf + ct)}$ and R$_b$ are conducive for good Li-cycling.

4. Conclusions

Single-phase CdFe$_2$O$_4$ with particle size, 100–200 nm is synthesized by urea combustion method followed by heating at 900°C for 6 h, and characterized by XRD, SEM, TEM and SAED techniques. The Li-cycling behaviour is examined by galvanostatic cycling and cyclic voltammetry (CV) in the range, 0·005–3·0 V vs Li at 0·07 C at room temperature. CdFe$_2$O$_4$ shows the first-cycle reversible capacity of 870 ($\pm$ 10) mAhg^{-1} that corresponds to 9·4 moles of Li per mole of CdFe$_2$O$_4$; however, the capacity fades at a rate of 4 mAhg^{-1} per cycle and retains only 680 ($\pm$ 10) mAhg^{-1} after 50 cycles. On the other hand, heat-treated electrode (300°C for 12 h in Ar) shows a significant improvement of the cycling performance, and a stable capacity of 810 ($\pm$ 10) mAhg^{-1} (8·7 moles of Li vs theoretical, 9·0 moles) is shown up to 60 cycles with coulombic efficiency 96–98%. Rate capability of heat-treated CdFe$_2$O$_4$ is also examined. Reversible capacities of 650 ($\pm$ 10) mAhg^{-1} and 450 ($\pm$ 10) mAhg^{-1} at 0·5 C (range 15–38 cycles) and 1·4 C (range, 56–75 cycles) (assuming 1 C = 840 mAhg^{-1}) are observed which are higher than the theoretical capacity of graphite (~ 372 mAhg^{-1}). The improved cycling performance of heat-treated electrode of CdFe$_2$O$_4$ is attributed to a more homogeneous distribution/dispersion of active material in the matrix of conducting carbon and good adherence to the current collector. From the CV data during 2–15 cycles, the average discharge potential is measured to be ~ 0·9V, whereas the charge potential is ~ 2·1 V. Based on the galvanostatic cycling, CV, *ex situ*-XRD, -TEM and -SAED studies, a reaction mechanism is proposed involving the alloying-de-alloying of (Li$_3$Cd) and conversion reactions of Cd and Fe (Cd $\leftrightarrow$ CdO and Fe $\leftrightarrow$ FeO). The measured impedance spectra during the first cycle have been fitted to an equivalent circuit and interpreted in terms of changes in the impedance parameters, viz. surface film, charge transfer and bulk impedances, and the associated CPEs. The Li-storage and cycling performance of CdFe$_2$O$_4$ is comparable to that of ZnCo$_2$O$_4$ and ZnFe$_2$O$_4$ and thus, may find use as an anode material for LIBs, but for the toxic nature of cadmium.

References

Armand M and Tarascon J -M 2008 *Nature* **451** 652
Chen J, Xu L, Li W and Gou X 2005 *Adv. Mater.* **17** 582

Cheng F, Tao Z, Liang J and Chen J 2008 *Chem. Mater.* **20** 667

Grugeon S, Laruelle S, Dupont L and Tarascon J -M 2003 *Solid State Sci.* **5** 895

Huang H, Faulkner T, Barker J and Saidi M Y 2009 *J. Power Sources* **189** 748

Larcher D, Masquelier C, Bonnin D, Chabre Y, Masson V, Leriche, J B and Tarascon J -M 2003 *J. Electrochem. Soc.* **150** A133

Lavela P and Tirado J L 2007 *J. Power Sources* **172** 379

Li Y, Tan B and Wu Y 2008a *Chem. Mater.* **20** 567

Li J, Dahn H M, Krause L J, Le D B and Dahn J R 2008b *J. Electrochem. Soc.* **155** A812

Manthiram A, Choi J and Choi W 2006 *Solid State Ionics* **177** 2629

Morales J, Sanchez L, Martin F, Berry F and Ren X 2005 *J. Electrochem. Soc.* **A152** 1748

Nazri G A and Pistoia G (eds) 2003 *Lithium batteries: science and technology* (New York: Kluwer Academic)

NuLi Y N, Chu Y Q and Qin Q Z 2004 *J. Electrochem. Soc.* **151** A1077

Padhi A K, Nanjundaswamy K S and Goodenough J B 1997 *J. Electrochem. Soc.* **144** 1188

Patil K C, Hegde M S, Rattan T and Aruna S T 2008 *Chemistry of nano-crystalline oxide materials* (Singapore: World Scientific)

Rao C N R 2005 *Int. J. Nanosci.* **4** 811

Rao C N R and Gopalakrishnan J 1986 *New directions in solid state chemistry* (UK: Cambridge University Press) Second edn. 1997

Rao C N R and Govindaraj A 2005 *Nanotubes and nanowires* (London: The Royal Society of Chemistry) Reprinted in 2007

Rao C N R and Kalyanikutty K P 2008 *Acc. Chem. Res.* **41** 489

Rao C N R, Kulkarni G U, Thomas P J and Gautam U 2003 *Curr. Sci.* (*India*) **85** 1041

Rao C N R, Muller A and Cheetham A K (eds) 2004 *Chemistry of nanomaterials* (Weinheim: Wiley-VCH) Reprinted in 2006

Rao C N R, Thomas P J and Kulkarni G U 2007a *Nanocrystals: synthesis, properties and applications* (Berlin: Springer-Verlag)

Rao C N R, Muller A and Cheetham A K (eds) 2007b *Nano-materials chemistry: recent developments and new directions* (Weinheim: Wiley-VCH)

Rao C N R, Vivekchand S R C, Biswas K and Govindaraj A 2007c *Dalton Trans.* **34** 3728

Rao C N R, Biswas K, Subrahmanyam K S and Govindaraj A 2009 *J. Mater. Chem.* **19** 2457

Reddy M V, Subba Rao G V and Chowdari B V R 2006 *J. Power Sources* **159** 263

Reddy M V, Yu T, Sow C H, Shen Z X, Lim C T, Subba Rao G V and Chowdari B V R 2007 *Adv. Funct. Mater.* **17** 2792

Reddy M V, Subba Rao G V and Chowdari B V R 2008 *Solid state ionics: new materials for pollution free energy devices*, in *Proceedings of the 11th Asian conference on solid state ionics* (eds) B V R Chowdari *et al* (New Delhi: MacMillan, India Ltd.)

Reddy M V, Subba Rao G V and Chowdari B V R 2009 (to be published)

Saravanan K, Reddy M V, Balaya P, Gong H, Chowdari B V R and Vittal J J 2009 *J. Mater. Chem.* **19** 605

Sharma Y, Sharma N, Subba Rao G V and Chowdari B V R 2007a *Adv. Funct. Mater.* **17** 2855

Sharma Y, Sharma N, Subba Rao G V and Chowdari B V R 2007b *J. Power Sources* **173** 495

Sharma Y, Sharma N, Subba Rao G V and Chowdari B V R 2008a *Electrochim. Acta* **53** 2380

Sharma Y, Sharma N, Subba Rao G V and Chowdari B V R 2008b *Solid State Ionics* **179** 587

Sharma Y, Sharma N, Subba Rao G V and Chowdari B V R 2009a *J. Mater. Chem.* (in press)

Sharma Y, Sharma N, Subba Rao G V and Chowdari B V R 2009b (unpublished results)

Shukla A K and Kumar T P 2008 *Curr. Sci.* (*India*) **94** 314

Sony press news: http://www.sony.net/SonyInfo/News/Press/200502/05-006E/index.html

Tirado J L 2003 *Mater. Sci. Eng.* **R40** 103

Wang J, King P and Huggins R A 1986 *Solid State Ionics* **20** 185